

RELIABILITY-BASED DESIGN OF TRUSS STRUCTURES BY ADVANCED ANALYSIS

HANNAH B BLUM

RESEARCH REPORT R936
MAY 2013

ISSN 1833-2781

SCHOOL OF CIVIL
ENGINEERING



THE UNIVERSITY OF
SYDNEY



THE UNIVERSITY OF
SYDNEY

SCHOOL OF CIVIL ENGINEERING

RELIABILITY-BASED DESIGN OF TRUSS STRUCTURES BY ADVANCED ANALYSIS

RESEARCH REPORT R936

HANNAH B. BLUM

May 2013

ISSN 1833-2781

Copyright Notice

School of Civil Engineering, Research Report R936
Reliability-Based Design of Truss Structures by Advanced Analysis
Hannah B. Blum
May 2013

ISSN 1833-2781

This publication may be redistributed freely in its entirety and in its original form without the consent of the copyright owner.

Use of material contained in this publication in any other published works must be appropriately referenced, and, if necessary, permission sought from the author.

Published by:
School of Civil Engineering
The University of Sydney
Sydney NSW 2006
Australia

This report and other Research Reports published by the School of Civil Engineering are available at <http://sydney.edu.au/civil>

ABSTRACT

A formwork for determining a system resistance factor in LRFD is presented. A truss composed of HSS members based on current design specifications is chosen for analysis.

To reflect real structures, the truss system is analyzed by advanced second order analysis, which takes into account the variation in physical properties and directly models geometric and material nonlinear behavior. Measured data on the variation of physical properties reported in literature is located including member imperfections, residual stresses, member thickness, Young's modulus and yield stress. Distributions of these values are obtained from data for recreation in the finite element models. Member imperfection profiles are generated and residual stress patterns through the thickness and around the cross-section are formulated. The variations of physical properties are represented in the finite element simulations using Latin Hypercube sampling of the random variables. Random loads are also modeled.

A connection modeling technique is devised, and finite element models of the structure are created and compared to benchmark tests to assess their validity. A 2D model of a single truss and a 3D model of a system of trusses are created. Simulations are completed to obtain strength distributions of each system, followed by a reliability analysis to determine resistance factors for each system. The results of the system analysis and resulting reliability index and system resistance factors are compared to that of component based design. It is found that the system resistance factor for the specific system analyzed herein is lower than that of the resistance factor for individual components.

KEYWORDS

Hollow structural sections, cold-formed steel, residual stresses, geometric imperfections, system reliability, finite element modeling

TABLE OF CONTENTS

ABSTRACT	3
KEYWORDS.....	3
TABLE OF CONTENTS.....	4
1 INTRODUCTION.....	5
2 PROPERTY AND MEMBER VARIATIONS	6
2.1 Thickness.....	6
2.2 Young's Modulus and Yield Stress.....	6
2.3 Implementation in Models.....	7
3 GEOMETRIC IMPERFECTIONS.....	7
3.1 Data	7
3.2 Modeling.....	8
3.3 Implementation in Models.....	11
4 RESIDUAL STRESSES.....	11
4.1 Distribution	11
4.1.1 Longitudinal	12
4.1.2 Transverse.....	12
4.2 Magnitude	14
4.2.1 Longitudinal	14
4.2.2 Transverse.....	16
4.3 Implementation in Models.....	17
5 MODELING	19
5.1 Joints.....	20
5.2 Inputs and Analysis	21
6 SYSTEM RELIABILITY.....	25
6.1 Background	25
6.2 Proposed System Reliability Method.....	26
6.3 Variability in Resistance	28
6.4 Failure Modes and System Effects.....	30
6.5 Variability in Resistance and Load.....	32
7 CONCLUSIONS	36
8 REFERENCES.....	37

1 INTRODUCTION

Hollow structural sections are typically cold-formed, seam welded, and rolled into the desired cross-sectional shape. Compared to open sections, HSS are more efficient in resistance to compression, torsion, and multi-axis bending, leading to lower-weight designs. Being closed, the area needed to be covered by paint is reduced, thereby extending corrosion protection. Architects tend to choose hollow sections for their aesthetic appeal. Common applications include pedestrian bridges, frame systems, and roof trusses for large buildings such as storage buildings, exhibition and fair halls, and stadiums (Wardenier et al., 2010). A common frame/truss system was chosen for analysis herein.

The current steel design process consists of two steps, an analysis to determine internal actions such as forces and moments, and a design check for adequate strength, for all individual members and connections. Component-based design is a simplistic process that could be improved to increase efficiency and economy. Advanced analysis completes the analysis and design check in a single step, thereby saving time in the design process. Additionally, advanced analysis directly models factors affecting the structure, such as geometric imperfections and residual stresses, enabling the user to accurately model the structure. Component-based design does not consider the system's ability to redistribute loads, and thus in systems where this is possible the true load carrying capacity is greater than predicted.

The current design code uses load and resistance factors to meet a specified level of reliability for each component. As system behavior is different than that of an individual component, the system reliability is not the same as the component reliability. Thus a system resistance factor must be determined in order for the system to meet a target reliability index. Enforcing a system reliability will create an economical system which is designed for a specified probability of failure.

This was part of a larger project currently in progress at the University of Sydney to study system-based reliability of frames using advanced second order advanced analysis. The study includes frames composed of hot-rolled steel, cold-formed steel, and their joints.

The work encompassed in this research report was completed as a requirement for the first author's Master's thesis (Blum, 2012) at the Johns Hopkins University.

2 PROPERTY AND MEMBER VARIATIONS

2.1 THICKNESS

Variability of thickness affects the strength of a member as it directly changes the cross sectional area available to resist internal forces due to loading. For this project, it was assumed that each member had a uniform thickness along its length for each of the four sides, but that the value of thickness relative to the nominal was random.

The variability of thickness in HSS members was obtained through recently collected data for a report to AISC which characterized dimensional variability in HSS members produced in the US (Christopher M. Foley, personal communication, February 7, 2011). This report contains data on the variation of several dimensional measurements, however only thickness data was utilized in this project. Samples were obtained from three HSS manufactures in the US for 6 typical cross sections, ranging in size from 12"x6" to 3"x3" and thicknesses from 5/8" to 3/16". There were a total of 28 samples measured and sample lengths ranged from 11 to 13 inches. Thickness measurements were taken at 16 locations around the cross section: 3 along each face and 1 at each corner at 1 inch from both ends of each specimen.

The thickness measured at each of the 32 locations along the samples was divided by the nominal thickness of the sample. A histogram of the 896 data points of actual thickness relative to nominal was created (Figure 2-1). The data has a mean of 0.964 actual to nominal, a standard deviation 0.039, and is represented by a normal distribution.

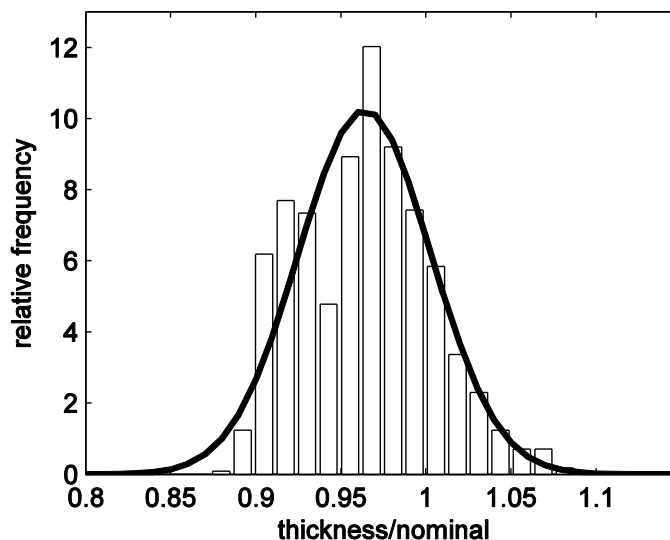


Figure 2-1: Histogram and normal PDF fit of HSS wall thickness

2.2 YOUNG'S MODULUS AND YIELD STRESS

Material properties such as Young's modulus, E , and yield stress, F_y , affect the strength of structural members by varying at which stress they begin to experience plastic deformations and at which strain this occurs.

Galambos and Ravindra's data on material properties used in LRFD criteria given in the September 1978 Journal of the Structural Division is widely used today. In lieu of current measurement data on the variation of Young's modulus and yield stress, their data was utilized. The nominal values of Young's modulus and yield stress utilized in the simulations, as well as their mean to nominal ratio and COV are given in the table below.

Table 2-1: Values of E and F_y in models

	Nominal (GPa)	Mean / nominal	COV
E	200	1.0	0.06
F _y	0.35	1.1	0.1

2.3 IMPLEMENTATION IN MODELS

Latin hypercube sampling was employed to reproduce values of thickness, Young’s modulus, and yield stress for chord and web members for all simulations. In the 2D models, all chord members were correlated, and all web members were correlated. This reflects how chord members and web members come from the same batch and have similar properties. Additionally, if all n members were uncorrelated, the variability would be much smaller than a single member’s variability as shown below (Eq. 2.1) where V is the coefficient of variation.

$$V_{system} = \frac{V_{member}}{\sqrt{n}} \quad (2.1)$$

Correlating some members produced a system variability between that of a single member and that of a fully uncorrelated system.

In the 3D models, all chord members in a truss were correlated and all web members in a truss were correlated, however the members were not correlated between trusses. Thus the 3D model was a system of independent trusses, and system behavior was observed through the simulations of systems of independent trusses.

3 GEOMETRIC IMPERFECTIONS

Structural members are not perfectly straight. Manufacturing processes introduce geometric imperfections which most often reduce the strength of members. It is important to model geometric imperfections as they heavily influence the behavior, strength, and stability in non-linear analyses. While there are several common methods utilized to account for the effects of geometric imperfections, for this project initial member imperfections were directly modeled in the finite element simulations by offsetting nodes from their original positions. As all members utilized were compact, effects due to local imperfections were insignificant and were ignored.

3.1 DATA

Geometric imperfection data collected consisted of three sets, one from the Milan University of Technology (Politecnico, 1966) and two from the University of Sydney: Wilkinson (1997) and Key (1988). Data collected was used to calculate the member imperfection.

The data from Milan University of Technology consisted of ten 6-foot (1,829.5 mm) square hollow sections measured prior to column testing. Bow-out imperfections were measured at the ends, middle, and quarter points along two adjacent faces to account for member imperfections along both axes. Effects of self-weight on the members were not apparent in the reported data. Data was analyzed to determine imperfection profiles relative to the ends of each member.

Data from Wilkinson, University of Sydney, 1997 consisted of 29 6-foot (2 m) rectangular hollow sections; however measurements were only taken from the middle 2 feet (0.6 m) or 1 foot (0.3 m) of each member. Eight readings, 2 at each face just inside the corners, were taken around the cross section at 1 inch (25 mm) intervals for two separate runs. The average of the two runs for each measurement was utilized. Data was analyzed to determine the member imperfection along both axes and to eliminate the effects of self-weight, and determine imperfection profiles relative to the ends of each member.

Data from Key, University of Sydney, 1988 consisted of six square hollow sections, varying in length from 8.9 feet (2717 mm) to 23.6 feet (7190 mm). Imperfection profiles relative to the ends were given about both axes for all specimens, with measurements at various intervals along the length of the member. The effects of self-weight were not apparent in the reported data.

3.2 MODELING

Geometric imperfections were modeled as a linear superposition of the first three eigen buckling modes ($n=1,2,3$):

$$\sin\left(\frac{n\pi x}{L}\right) \quad (3.1)$$

where L is the length of the member and x is the location along the length of the member. Scale factors, δ_1 , δ_2 , and δ_3 , represent the contribution of each mode (1st, 2nd, and 3rd, respectively) to the overall imperfection shape, which was normalized to a maximum value of 1 (Figure 3-1).

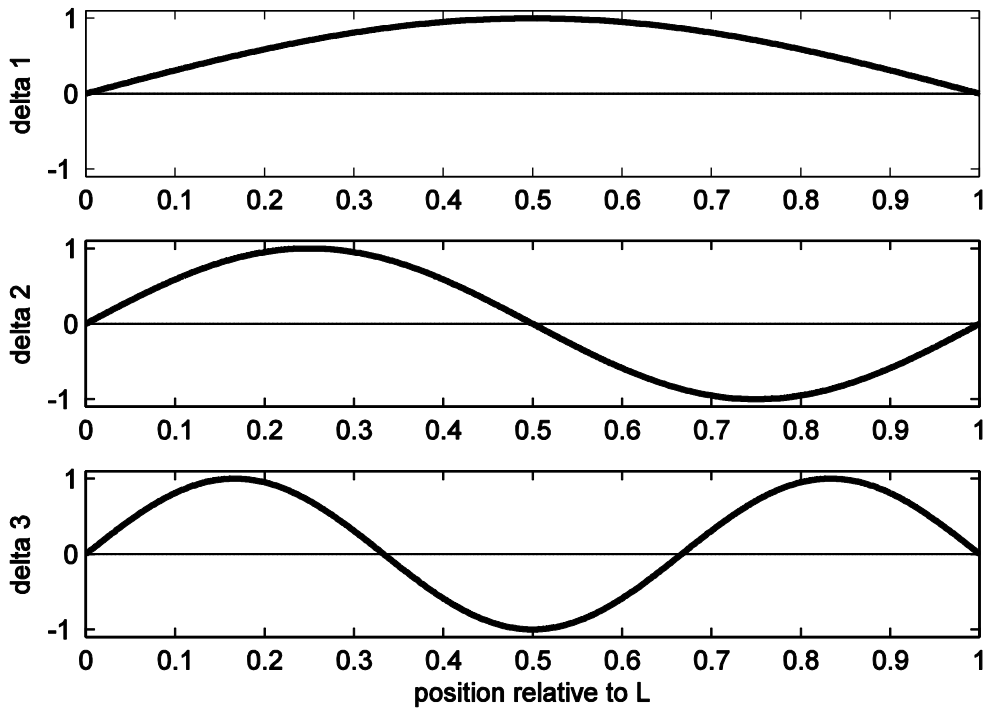


Figure 3-1: Eigen buckling mode shapes for 1st, 2nd, and 3rd mode

For the data from the Milan University of Technology, imperfections at the quarter points and midpoint were known, so the following set of equations were solved to determine δ_1 , δ_2 , and δ_3 for imperfection profiles about both axes of each member:

$$\delta_{0.25} = \delta_1 \sin\left(\frac{\pi}{4}\right) + \delta_2 \sin\left(\frac{\pi}{2}\right) + \delta_3 \sin\left(\frac{3\pi}{4}\right) \quad (3.2)$$

$$\delta_{0.5} = \delta_1 \sin\left(\frac{\pi}{2}\right) + \delta_2 \sin(\pi) + \delta_3 \sin\left(\frac{3\pi}{2}\right) \quad (3.3)$$

$$\delta_{0.75} = \delta_1 \sin\left(\frac{3\pi}{4}\right) + \delta_2 \sin\left(\frac{3\pi}{2}\right) + \delta_3 \sin\left(\frac{9\pi}{4}\right) \quad (3.4)$$

The results of $\bar{\delta}_1$, $\bar{\delta}_2$, and $\bar{\delta}_3$ were divided by the length of the members to obtain distributions of $\bar{\delta}_1/L$, $\bar{\delta}_2/L$, and $\bar{\delta}_3/L$.

Both sets of data from the University of Sydney have measurements taken at various intervals along the length of the member. To solve for the scale factors, error between the measured imperfection at any location along the member and the reproduced imperfection calculated by the combinations of the first three eigen buckling modes was minimized. Error is calculated as:

$$E = \sum_{x=0}^L \left[r_x - (a_x \delta_1 + b_x \delta_2 + c_x \delta_3) \right]^2 \quad (3.5)$$

where x is the location along the member, $0 \leq x \leq L$, r_x is the measured imperfection at location x , and a_x , b_x , and c_x are the values of the 1st, 2nd, and 3rd modes, respectively, at location x assuming the maximum value of each buckling shape is one. Solving the following equation yields solutions for $\bar{\delta}_1$, $\bar{\delta}_2$, and $\bar{\delta}_3$:

$$\frac{\partial E}{\partial \delta_1} = \frac{\partial E}{\partial \delta_2} = \frac{\partial E}{\partial \delta_3} = 0 \quad (3.6)$$

Error minimization was performed for imperfection profiles for both axes of each member, and divided by the length of the measured section to obtain distributions of $\bar{\delta}_1/L$, $\bar{\delta}_2/L$, and $\bar{\delta}_3/L$.

Following the above mentioned procedure, distributions of $\bar{\delta}_1/L$, $\bar{\delta}_2/L$, and $\bar{\delta}_3/L$ were obtained for all members about both axes. As it is unknown how each member is oriented, especially in the case of square hollow sections, imperfections about the different axes were considered as separate data points. Thus, the data set consisted of ninety samples for each of the three buckling modes. Additionally, the sign of $\bar{\delta}_1/L$, $\bar{\delta}_2/L$, and $\bar{\delta}_3/L$ represented an arbitrary sign convention of either up or down from the horizontal, based on how the member was oriented when measured. However, imperfection direction is arbitrary and has an equal chance of occurring in either direction, thus only the magnitude of $\bar{\delta}_1/L$, $\bar{\delta}_2/L$, and $\bar{\delta}_3/L$ are important. Histograms of the magnitude of $\bar{\delta}_1/L$, $\bar{\delta}_2/L$, and $\bar{\delta}_3/L$ were created along with their lognormal distribution fits and are shown in Figure 3-2, Figure 3-3, and Figure 3-4.

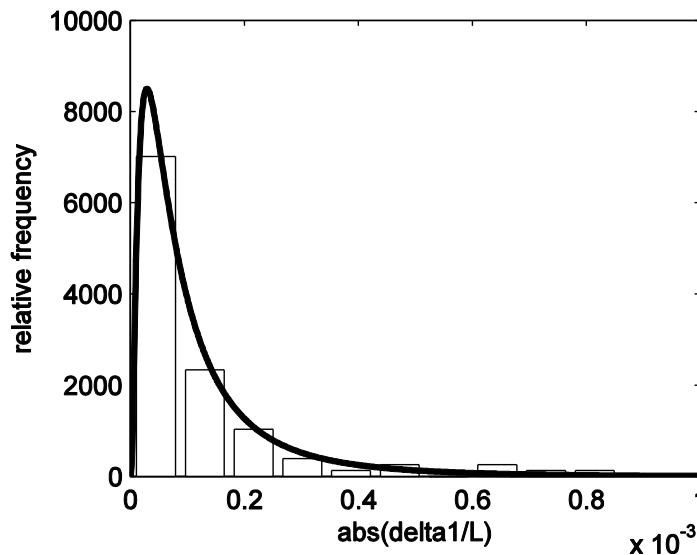


Figure 3-2: Histogram and lognormal PDF of the magnitude of $\bar{\delta}_1/L$

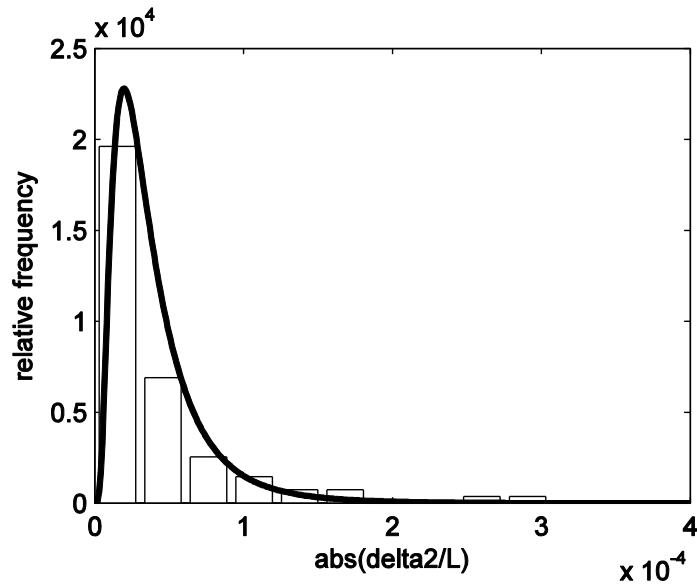


Figure 3-3: Histogram and lognormal PDF fit of the magnitude of δ_2/L

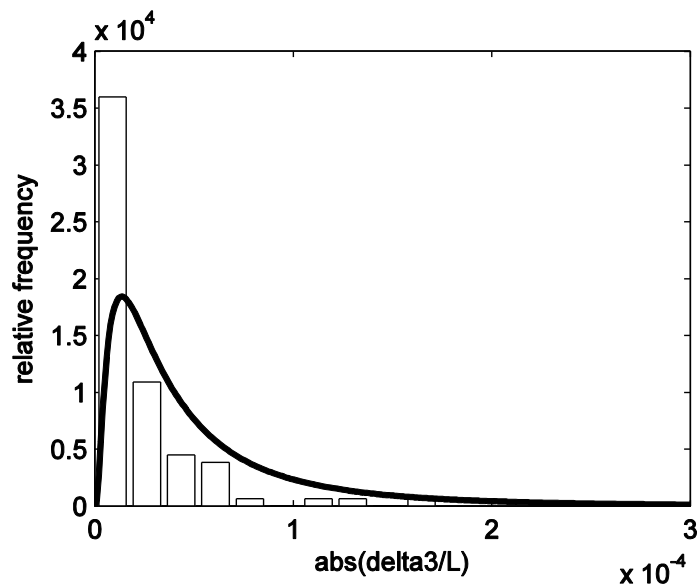


Figure 3-4: Histogram and lognormal PDF fit of the magnitude of δ_3/L

The mean, standard deviation, and COV of the magnitude of δ_1/L , δ_2/L , and δ_3/L are shown in Table 3-1.

Table 3-1: Scale factors distribution results for member imperfections

	$abs(\delta_1/L)$	$abs(\delta_2/L)$	$abs(\delta_3/L)$
Mean (μ)	1.26E-4	4.08E-5	2.20E-5
St. dev. (σ)	1.62E-4	5.16E-5	2.81E-5
C.O.V.	1.29	1.26	1.27
$\delta \approx L/x$	$\delta_1 \approx L/8000$	$\delta_2 \approx L/25000$	$\delta_3 \approx L/45000$

Based on the relative magnitudes of δ_1/L , δ_2/L , and δ_3/L , imperfection profiles were more heavily influenced by the 1st mode, followed by the 2nd mode, and then the 3rd mode. The coefficient of variation is large due to the very small mean of the scale factors. The mean of δ_1 is comparable to an imperfection of $L/8000$, which is 8

times smaller than the maximum permissible tolerance of $L/1000$ for bow according to AISC's Code of Standard Practice, 2000 (Buonopane, 2008).

It was determined that a lognormal distribution would be used to model the variability in the magnitude of the imperfection scale factors as it most closely fit the data among the commonly used distribution function. It is important to note that the lognormal function does not accurately portray the data, as it shows a zero probability of a section having no imperfection. The histograms of δ/L most closely resembled a Cauchy distribution centered around zero. Clearly there is a possibility of a member having no imperfection, however, making it impossible for a member to have no imperfection is conservative, and thus is desirable for design.

3.3 IMPLEMENTATION IN MODELS

To represent member imperfection profiles in the FE simulations, Latin Hypercube sampling was employed to reproduce the scale factors (δ_1/L , δ_2/L , and δ_3/L) from the above lognormal distributions for each member in each simulation. Next, a random sign was generated (either +1 or -1) for each scale factor for each member to represent the direction of the imperfection. As a result, every member in every simulation had a randomly generated imperfection profile.

The value of the nodal imperfection perpendicular to the member, u , along the length of the member is calculated as follows:

$$u\left(\frac{x}{L}\right) = L \left[s_1 \left(\frac{\delta_1}{L} \right) \sin\left(\frac{\pi x}{L}\right) + s_2 \left(\frac{\delta_2}{L} \right) \sin\left(\frac{2\pi x}{L}\right) + s_3 \left(\frac{\delta_3}{L} \right) \sin\left(\frac{3\pi x}{L}\right) \right] \quad (3.7)$$

where x/L is the location of each node relative to the length of the member from $0 \leq x \leq L$, s_1 , s_2 , and s_3 are randomly generated signs represented by either +1 or -1, and δ_1/L , δ_2/L , and δ_3/L are the randomly generated scale factors from the aforementioned distributions.

For the 2D simulations, only in-plane member imperfection profiles were generated as out-of-plane displacements were restricted. For the 3D simulations, member imperfections were considered about both cross-sectional axes. As there was no evidence in the data of imperfections about one axis correlating to imperfections about the other axis, separate member imperfection profiles were generated for each axis of all members.

4 RESIDUAL STRESSES

The formation of cold-formed hollow sections produces a complex distribution of residual stresses. The sections are formed by uncoiling and leveling sheets of steel. They are next roll formed into tubes and seam-welded, then sized into the required shape (Li et al., 2008). Specifically there are two methods for forming rectangular hollow sections, one by directly forming the rectangular section from the sheet, the other by forming a circle cross section from the sheet, then forming the circle into the final rectangular cross section (Li et al., 2009). The processes of uncoiling and leveling, roll-forming, and sizing produce residual stresses in both the longitudinal and circumferential directions, which affect the strength of the tubes (Kato and Aoki, 1978).

To model residual stress in the FE models, data was separated into longitudinal and transverse components. Residual stress distributions through the thickness and around the cross section and magnitudes of the residual stresses were determined based on models and experimental data found in literature.

Although the data regarding residual stress distributions in cold-formed hollow sections is sparse, several distributions were analyzed to determine the best model to implement in the simulations.

4.1 DISTRIBUTION

4.1.1 Longitudinal

There were several models in the literature for longitudinal residual stress in HSS. The distributions were similar, but the model proposed by Davison and Birkemoe (1982) was chosen for its simplicity in defining an equation to represent the distribution. They experimentally measured residual stresses from coupons and determined a model to reflect the data and theory. Davison and Birkemoe (1982) determined that there are two residual stress gradients in the longitudinal direction, one across the tube face and around the cross section, denoted as membrane, and the other perpendicular to the tube face through the material thickness, denoted as bending. "The perimeter (membrane) residual stress gradient represents the variation in the mean value of the longitudinal residual stress [and] the through thickness (bending) residual stress gradient is the deviation from this mean value normal to the perimeter through the material thickness" (Davison and Birkemoe, 1982). In their model, bending is symmetrical through the thickness, with tension at the outer face and compression at the inner face (Figure 4-1(a)), and membrane residual stress is constant through the thickness (Figure 4-1(b)). They found that the maximum magnitude of through thickness residual stresses was less for coupons taken from the corners than for coupons taken from the flats (Davison and Birkemoe, 1982). Key and Hancock (1993) also confirmed that longitudinal bending through thickness residual stresses were smaller in magnitude in the corner than flats, specifically that the corners have half the value as the flats (Figure 4.3(a)). The numbers reflecting the location along the cross-section is depicted in Figure 4-2. Membrane residual stresses vary linearly along the cross section (Figure 4.3(b)). The stress magnitudes are equal for the flats and corners, but vary from maximum tensile stress at the flat centerline to maximum compressive stress at the corner (Davison and Birkemoe, 1982). The distributions through the thickness and across the section produce no net force as shown in Eq. (4.1) where σ_b is the bending residual stress and σ_m is the membrane residual stress.

$$\int (\sigma_b + \sigma_m) dA = 0 \quad (4.1)$$

4.1.2 Transverse

Transverse residual stress data for HSS members in the literature was minimal. The distribution proposed by Key and Hancock (1993) was chosen to model transverse residual stresses (Figure 4-1(c)), which consists of tension at the outer surface and compression at the inner surface for the bending component, and zero for the membrane component. The relationship between values at the outer surfaces to values on the plateaus was determined by enforcing the requirement of no net force on the section. This resulted in the stress on the plateau being equal to 0.61 times the surface stress. Data from Li et al. (2008), which was determined experimentally by X-ray diffraction, shows that the transverse residual stresses in the corners is a third of the transverse residual stresses in the flats. Figure 4-3(c) depicts the transverse residual stress distribution around the section.

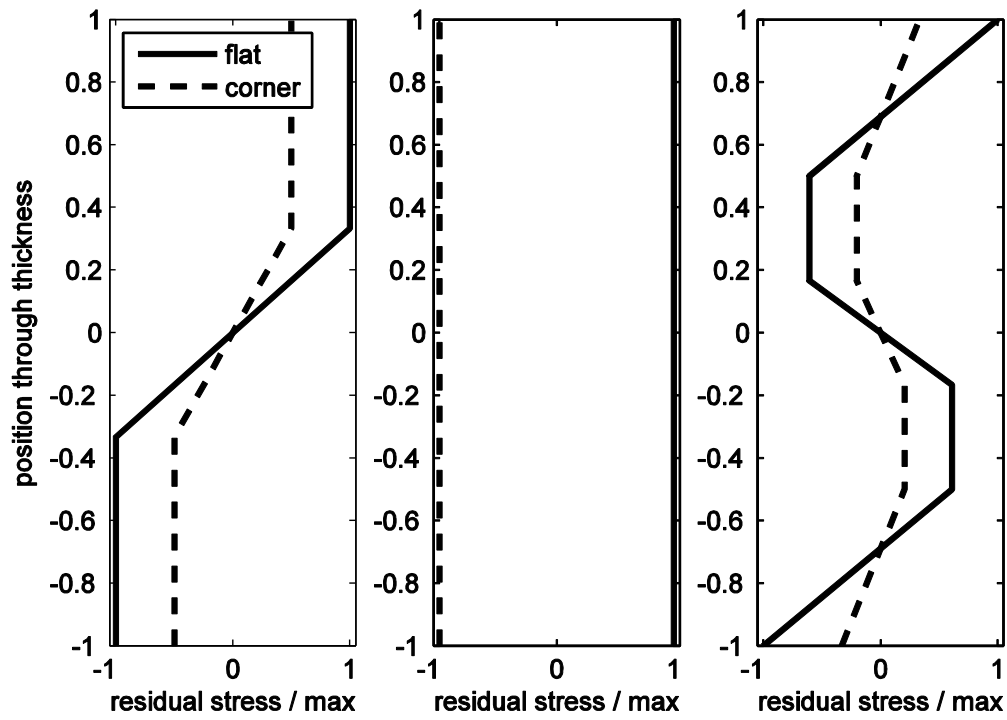


Figure 4-1: Through thickness residual stress distribution for (a) longitudinal bending, (b) longitudinal membrane, and (c) transverse

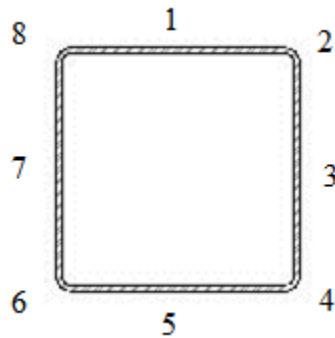


Figure 4-2: Square HSS numbered cross section points for reference in Figure 6

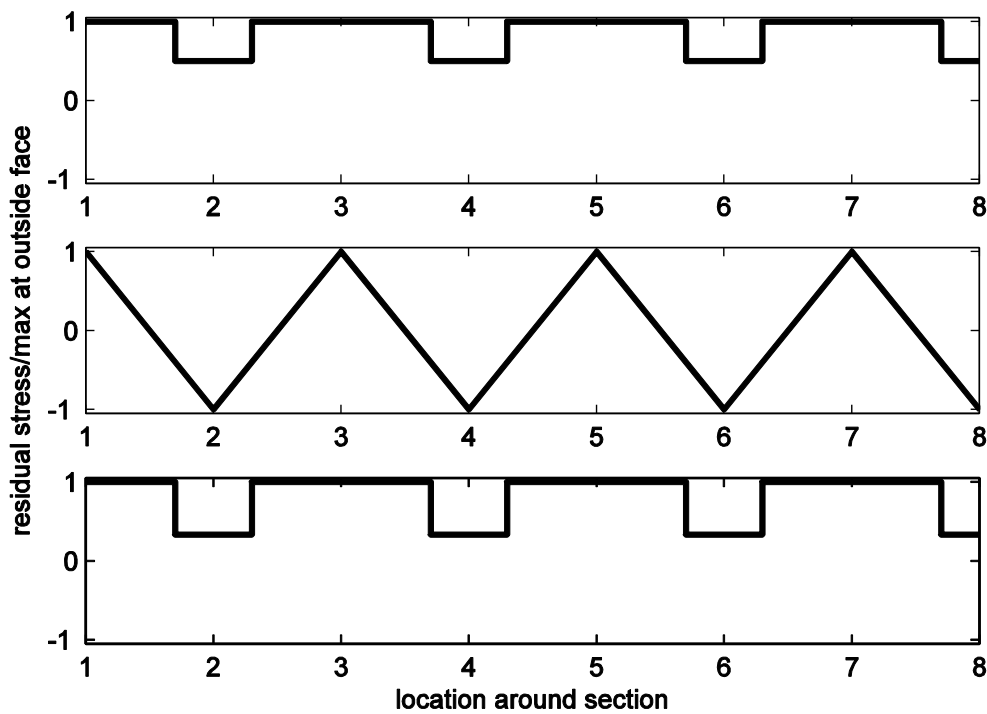


Figure 4-3: Residual stress distribution around cross-section at outside face for (a) longitudinal bending, (b) longitudinal membrane, and (c) transverse. Location numbers correspond to Figure 7

4.2 MAGNITUDE

4.2.1 Longitudinal

Davison and Birkemoe (1983) produced a set of experimental surface residual stress measurements for both the membrane and bending components for the flats and corners. This is shown in Table 4-1 along with the values from their model. These values confirm the previously stated assumptions that the membrane value is approximately equal in magnitude for the corner and flats but tensile for flats and compressive for corners, and that the bending component in the corners is approximately half the value of the flats. The histograms of the magnitude of longitudinal membrane component and outer surface longitudinal bending residual stress component for flat sections are shown in Figure 4-4 and Figure 4-5 respectively. The magnitude of the longitudinal membrane component is best modeled by a lognormal distribution while the outer surface longitudinal bending residual stress is best modeled by a normal distribution. The distribution parameters are given in Table 4-4.

Table 4-1: David and Birkemoe (1982) surface residual stress measurements (%F_y)

Surface residual stresses		Flat	Corner
Experimental (flat – 35 samples) (corner – 12 samples)	Membrane	0.11	-0.15
	Bending	0.71	0.39
Model	Membrane	0.17	-0.17
	Bending	0.60	

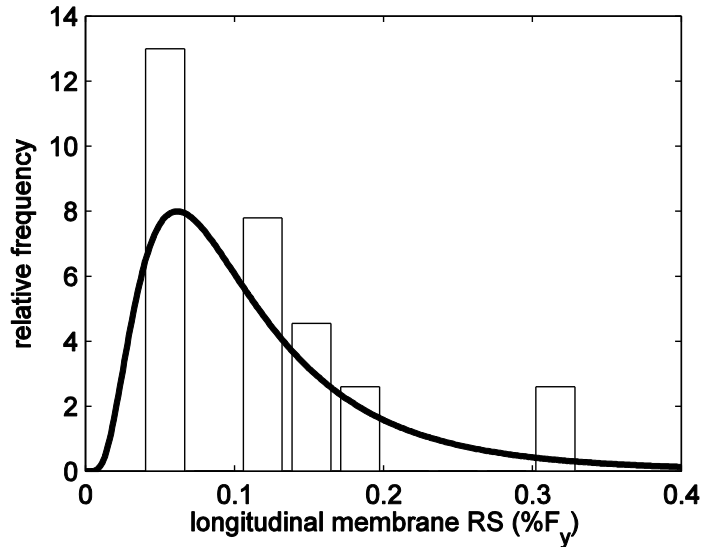


Figure 4-4: Histogram and lognormal PDF fit of the magnitude of longitudinal membrane residual stress as a percent of yield stress

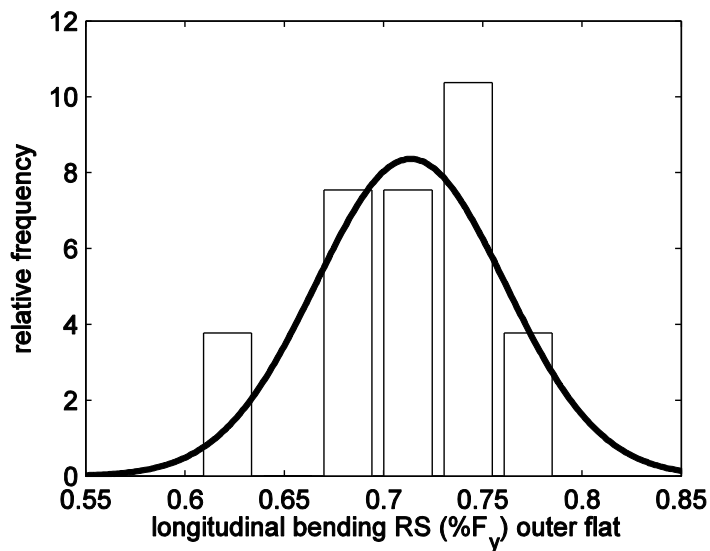


Figure 4-5: Histogram and normal PDF fit of outer surface longitudinal bending residual stress as a percent of yield stress for flat section

As there was not enough data for the corners, the longitudinal membrane component for the corner was taken as the negative of the magnitude of lognormal membrane component obtained from the distribution, and the outer longitudinal bending component for the corner was taken as half the value obtained from the outer surface longitudinal bending residual stress component for the flats.

To compare with surface measurements obtained by X-ray diffraction from Li et al. (2008), the bending and membrane components measured by Davison and Birkemoe (1982) were added together, and the results are shown in Table 4-2. These results are consistent with the model derived above as the membrane is equal in magnitude but opposite in sign for the flat and corner, and the bending component for the corner is approximately half the value of the flat.

Table 4-2: Longitudinal outer surface residual stress (%F_y)

		Flat	Corner
Davison and Birkemoe (experimental)	Mean	0.82	0.24
	# samples	35	12
Li et al.	Mean	0.83	0.60
	# samples	5	3
Combined	Mean	0.82	0.32
	# samples	40	15
Final	Component	Flat	Corner
	Total	0.8	0.3
	Membrane	0.1	-0.1
	Bending	0.7	0.4

4.2.2 Transverse

The value obtained by Key and Hancock (1993) for transverse residual stress was compared to measured values by Li et al. (2008) using x-ray diffraction (Table 4-3). Although the through thickness distribution obtained by Li et al. (2008) varied slightly from Key and Hancock's (1993) distribution, both were similar in that the maximum value of transverse residual stress occurred on the surface, thus measurements were compared.

Table 4-3: Transverse outer surface residual stress (%F_y)

		Flat	Corner
Key and Hancock	Mean	0.50	–
	# samples	1	–
Li et al.	Mean	0.49	0.16
	# samples	5	3
Combined	Mean	0.49	0.16
	# samples	6	3
Final	Flat	Corner	
	0.5	0.2	

A histogram for the transverse outer surface residual stress for flats is shown in Figure 4-6. The variation was modeled as a normal distribution, with parameters given in Table 4-4. As there was not sufficient data for transverse residual stress for corners, its value was taken as one third that of the flat.

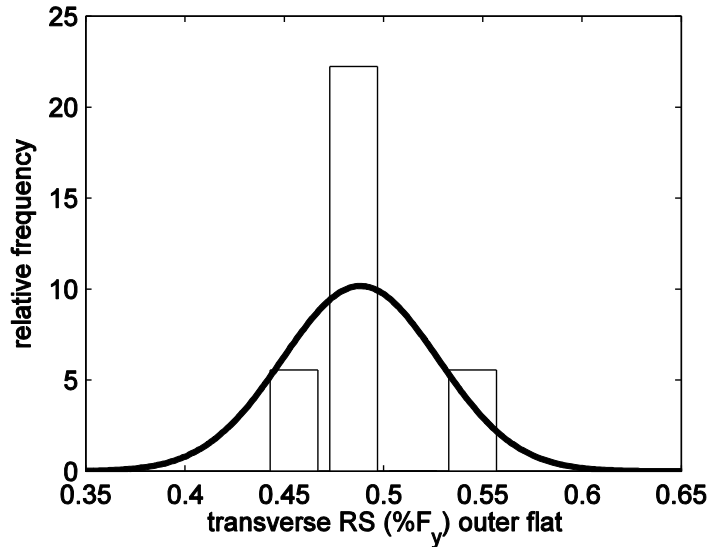


Figure 4-6: Histogram and normal PDF fit of outer surface transverse residual stress as a percent of yield stress for flat section

4.3 IMPLEMENTATION IN MODELS

A lognormal distribution was obtained for longitudinal membrane residual stresses, and normal distributions were obtained for longitudinal bending flat and transverse flat residual stresses. This was based on the limited amount of data collected, thus these distribution fits may not be accurate. More accurate probability distribution function fits can be obtained with greater samples of data. Due to the uncertainty in the data, only one significant figure was used for the mean and standard deviation, as reported in Table 6. The values represent the percent of the yield stress.

Table 4-4: Residual stress distribution parameters

Type	μ (% F_y)	σ	Distribution
Longitudinal membrane	0.1	0.08	lognormal
Longitudinal bending flat	0.7	0.05	normal
Transverse flat	0.5	0.04	normal

To produce surface residual stress values for longitudinal and transverse components for the flat and corner regions, values for longitudinal membrane, longitudinal bending flat, and transverse flat were obtained from the above distributions, and combined as follows in Table 7.

Table 4-5: Residual stress components for flat and corner

Region	Component	Calculation
Flat	Longitudinal	Longitudinal bending flat + longitudinal membrane
	Transverse	Transverse flat
Corner	Longitudinal	1/2 longitudinal bending flat – longitudinal membrane
	Transverse	1/3 transverse flat

Membrane residual stresses can be modeled in ABAQUS using the SIGINI subroutine by defining a value of the initial stress at each section point along the beam cross section. Unfortunately, the drivers and compilers needed to run the subroutine through ABAQUS were unavailable on the computing cluster at the time, and were therefore ignored in the modeling.

Through thickness residual stresses cannot be directly modeled in ABAQUS with beam elements. It was incorporated into the models through a modified stress strain curve. For simplicity in analytically defining the

material curve, transverse through thickness residual stresses were ignored, and only longitudinal bending through thickness residual stresses were taken into account.

The elastic-plastic material curve without the effects of residual stresses is defined by elastic (Eq. 4.2) and plastic (Eq. 4.3) components.

$$\sigma = E \varepsilon, \text{ for } 0 \leq \varepsilon \leq \frac{F_y}{E} \quad (4.2)$$

$$\sigma = F_y, \text{ for } \varepsilon \geq \frac{F_y}{E} \quad (4.3)$$

Through thickness residual stresses cause a rounding of the stress strain curve (Figure 4-7). For the virgin material, all fibers reach yield stress at the same strain, $\varepsilon_y = F_y/E$, whereas in material with residual stresses, fibers reach the yield stress at different levels of strain. For a member in tension, fibers with the maximum tensile residual stress yield first, at a strain smaller than ε_y . As the member is further loaded, other fibers yield when the sum of the stress due to loading and residual stress equals the yield stress. Fibers with compressive residual stresses yield at a strain larger than ε_y as the initial compression counteracts the tensile forces. Eventually the cross section will fully yield and will experience strain hardening. The converse is true for members in compression.

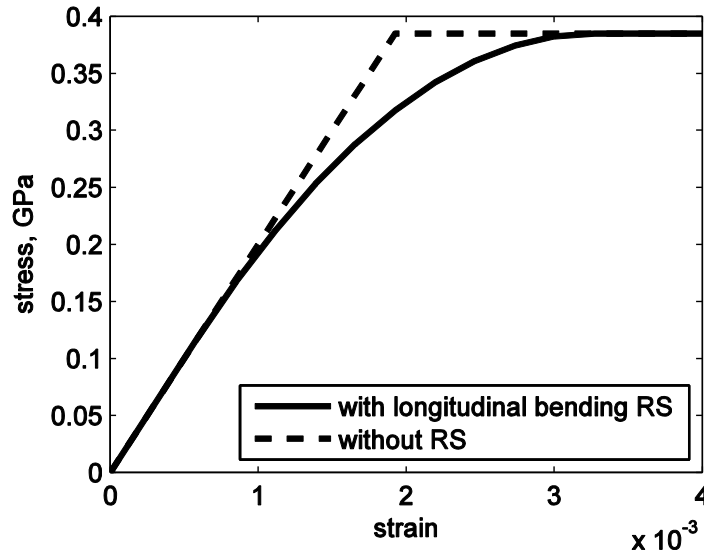


Figure 4-7: Stress-strain curve with and without the effects of residual stresses

The modified stress-strain curve incorporating the effects of residual stresses is modeled as follows (Eq. 4.4 – 4.6):

$$\sigma = E \varepsilon, \text{ for } 0 \leq \varepsilon \leq \varepsilon_1 \quad (4.4)$$

$$\sigma = A\varepsilon^3 + B\varepsilon^2 + C\varepsilon + D, \text{ for } \varepsilon_1 \leq \varepsilon \leq \varepsilon_2 \quad (4.5)$$

$$\sigma = F_y, \text{ for } \varepsilon \geq \varepsilon_2 \quad (4.6)$$

where ε_1 and ε_2 are defined in Eq. 4.7 and 4.8 and σ_b is the value of the outer surface longitudinal bending residual stress.

$$\sigma_b + E\varepsilon_1 = F_y \quad (4.7)$$

$$-\sigma_b + E\varepsilon_2 = F_y \quad (4.8)$$

To solve for the four unknowns, A, B, C, and D, four initial conditions must be satisfied. Both the slopes and stresses at $\varepsilon = \varepsilon_1$ and at $\varepsilon = \varepsilon_2$ are known (Eq. 4.9 – 4.13).

$$\frac{\partial \sigma}{\partial \varepsilon} = 3A\varepsilon^2 + 2B\varepsilon + C \quad (4.9)$$

$$\left. \frac{\partial \sigma}{\partial \varepsilon} \right|_{\varepsilon=\varepsilon_1} = E \quad (4.10)$$

$$\left. \frac{\partial \sigma}{\partial \varepsilon} \right|_{\varepsilon=\varepsilon_2} = 0 \quad (4.11)$$

$$\sigma(\varepsilon_1) = E\varepsilon_1 \quad (4.12)$$

$$\sigma(\varepsilon_2) = F_y \quad (4.13)$$

Solving the four simultaneous equations yields solutions for A, B, C, and D (Eq. 4.14).

$$\begin{bmatrix} 3\varepsilon_1^2 & 2\varepsilon_1 & 1 & 0 \\ 3\varepsilon_2^2 & 2\varepsilon_2 & 1 & 0 \\ \varepsilon_1^3 & \varepsilon_1^2 & \varepsilon_1 & 1 \\ \varepsilon_2^3 & \varepsilon_2^2 & \varepsilon_2 & 1 \end{bmatrix} \begin{bmatrix} A \\ B \\ C \\ D \end{bmatrix} = \begin{bmatrix} E \\ 0 \\ E\varepsilon_1 \\ F_y \end{bmatrix} \quad (4.14)$$

With these values known, Eq. 4.5 was determined and the full stress-strain curve defined.

5 MODELING

Rectangular HSS are much preferred to circular HSS because joint fabrication is easier. For RHS connections only straight bevel cuts are needed, whereas CHS connections must be profile cut after the tubes are fitted together and require a varied bevel cut for welding. Additionally, the flat sides of RHS are desirable for attaching deck and paneling to the trusses, and can be stacked for ease of handling (Packer et al., 2009).

Members come in a variety of thicknesses which affect their buckling behavior: compact, non-compact, and slender. Member thicknesses were chosen to have compact shapes so local buckling would not affect the strength of the system. Additionally, advanced analysis requires the members to be capable of plastic redistribution. In order to form a plastic collapse mechanism, sections must be capable of sustaining large rotations and displacements prior to failure. One of the criteria in AISC LRFD for suitability of plastic design is that the sections must be compact. Members were checked that they met AISC compact criteria so that local buckling would not affect strength, and provided that they meet the other provisions, were suitable for plastic design.

Joints are expensive to fabricate, thus trusses with less joints are cheaper. Warren trusses with K joints are much preferred over Pratt trusses with N joints. Additionally, gap joints are easier to construct than overlap joints (Wardenier et al., 2010).

Therefore, a Warren truss with K joints composed of rectangular hollow sections was selected. The example Warren truss from the RHS CIDECT design guide (Packer et al., 2009) was chosen since it met the above criteria and is a realistic truss one might encounter.

For 3D simulations, there were six trusses spaced at 15 m intervals. The total area under the truss system (36 m x 75 m or 118 ft x 246 ft) is sufficient to cover an indoor soccer field, and thus is a realistic layout. The trusses were connected by lateral bracings to prevent lateral torsional effects and aid load distribution between the trusses.

The aforementioned random variables – geometric imperfections, member thickness, Young’s modulus, yield stress, and residual stresses, are all on a member by member basis. However, a system is a collection of individual members which interact with one another. Thus simply analyzing how variations in properties create variability in the strength of a single member is not sufficient; the variability in the strength of the entire system as a result of individual member variations must be analyzed.

However, the strength of the system depends on its ability of lack thereof to redistribute loads. When a structural member reaches its fully plastic capacity, it will fail and form a plastic hinge. If the system has the ability and capacity to redistribute loads, additional load can be applied until a plastic collapse mechanism is formed and the entire structure fails. If the system cannot redistribute loads, the system will fail with the first failing member. A system with a low capacity to redistribute loads resembles a series system, while a system with a high ability to redistribute loads resembles a parallel system.

5.1 JOINTS

The first trusses consisted of individual members connected with steel pins. As these trusses were fully pinned, designers used statics to determine member axial forces. Later, truss designs changed and had continuous chords, however since the stiffness of connections were unknown, a pin-jointed analysis was still used. As computers came into use, designers used a plane-frame analysis to determine internal forces and moments, but only if the moment-rotation relationship between every connection was known. Since this data is not available for most joints, there are two main analysis techniques: either assume that all the members are pin-connected or assume that the truss has a continuous chord with pin-connected web members (Cran, 1989).

Modeling assumptions make design feasible in the absence of joint information; however it does not accurately portray the behavior of the structure. Different modeling assumptions may under or overestimate axial forces, internal moments, and deflections. It is important to compare the various models with experimental data to determine which produces the most accurate results.

There are three common modeling types: pinned, rigid, and pin-rigid. In the pinned model, all joints are pin-connected and can only transfer axial forces, whereas in the rigid model all joints are rigidly connected and can transfer in-plane axial, bending moment, and shear forces. In the pin-rigid model, the web members are pin-connected to continuous chords. The eccentricity between the web member centerlines and the chord centerlines are modeled as a stiff links (Figure 5-1).

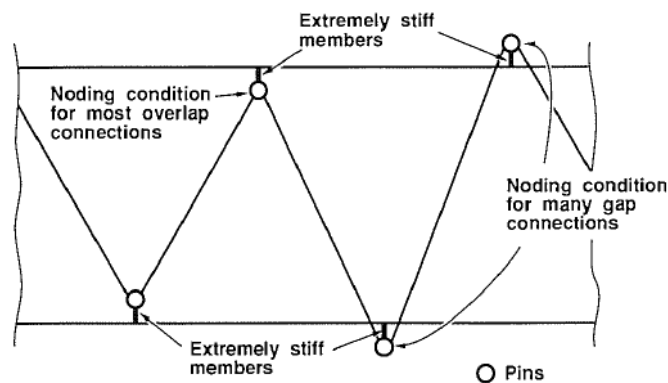


Figure 5-1: Pin-rigid model from Frater and Packer's "Modeling of hollow structural steel sections" (1992)

In the pin-rigid model, model lines coincide with member centerlines, thus the true web to chord angle is maintained. This is a benefit over the pinned and rigid models where the web to chord angle must be changed for eccentrically noded joints. Noding eccentricities cause bending moments, however these can be ignored if they are within the eccentricity limits as defined by the International Institute of Welding (Frater and Packer, 1992). The end fixities of the web members cause secondary bending moments, however these can also be ignored if there is adequate deformation capacity in both members and joints to allow for stress redistribution after local yielding of the joint (Frater and Packer, 1992).

The author devised another modeling technique where the web is pinned connected to the outside face of the chord, and a rigid link connects the outside face of the chord to the chord centerline (Figure 5-2). This reflects how the web is connected to the chord face, and hence that is where forces are transmitted to the chord cross-section.

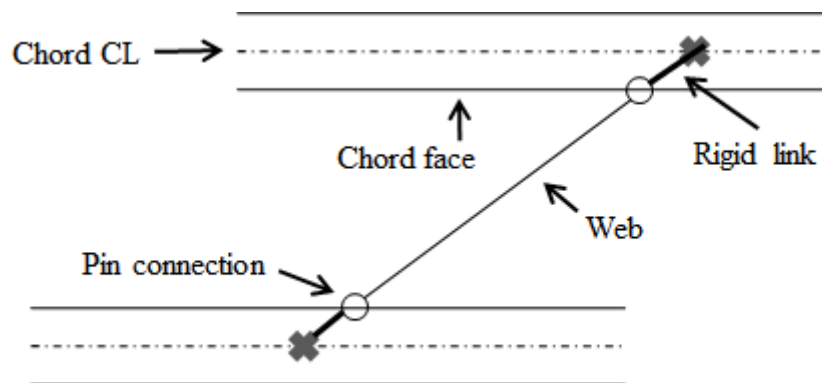


Figure 5-2: Author's connection modeling technique

Prior to obtaining any realistic finite element results from truss models, it was necessary to complete a mesh convergence study. The mesh density required to produce convergent results was determined, and this mesh density was used in all subsequent finite element models.

In order to confirm that the connection modeling technique in Figure 5-2 led to correct results, a finite element model was created of a full scale experimental truss test and results were compared. The truss test selected was from Frater and Packer (1992) in which a full scale Warren truss made of rectangular HSS members was tested in the elastic range. The axial forces and bending moments in the chords and webs produced in the experiment were approximately the same as those produced in the finite element model. Thus it was concluded that connection modeling technique in Figure 5-2 yielded appropriate results.

5.2 INPUTS AND ANALYSIS

The aforementioned random variables (E , F_y , t , geometric imperfections, residual stresses (σ_r)) affect the resistance of truss. However, there is also a variation in the applied loads. Random loads proposed by Ellingwood and Galambos (1982) were utilized in the simulations and are presented in Table 8.

Table 5-1: Random loads

Load	Mean / Nominal	C.O.V.	Distribution
Dead Load, D	1.05	0.10	Normal
Live Load, L 50 year maximum	1.0	0.25	Extreme type I
Live Load, L_{apt} Point-in-time	0.25	0.55	Gamma
Snow Load, S 50 year maximum	0.82	0.26	Extreme type II

Monte Carlo simulation is the most straightforward method to generate random data from a known distribution. However, it requires a large sample number in order to accurately reproduce the distribution. Instead, Latin Hypercube sampling was employed to reduce the number of simulations required to reproduce the distribution. In this sampling technique, the area under the probability distribution function is divided into N strata of equal area, hence equal probability of occurrence. For instance, areas under the tail of the PDF have wider strata while areas under the peak have narrow strata. Therefore there are more strata in the vicinity of the peak than in tails, reflecting how more of the data is located under the peak and less under the tails. Next, a random value is selected from each of the N intervals as a representative value for each strata. If the number of intervals is large, the mid-point of each strata can be selected instead of random sampling (Nowak and Collins, 2000). Each representative value is randomly selected and used only once (no repeated values) for all N simulations, thereby effectively randomly reproducing the given distribution. The recreation of the

distribution of Young's Modulus using Latin Hypercube simulation is shown in in Figure 5.3. Note that for N=350, the normal distribution is accurately recreated. As N=350 was sufficient to reproduce distributions for other variables, it was concluded that 350 simulations was sufficient for each truss system.

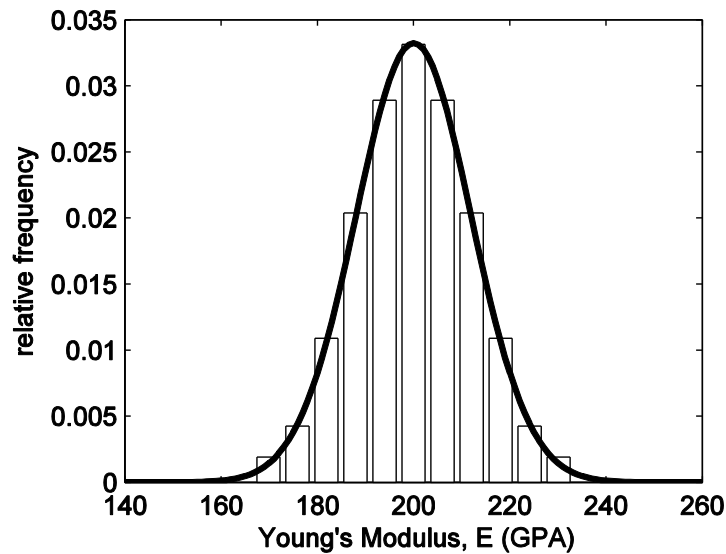


Figure 5-3: Variation in E using Latin Hypercube sampling for N=350

As stated previously, the truss design example by CIDECT (Packer et al., 2009) was selected for modeling. The truss layout and loads applied is shown in Figure 5-4. However, some modifications were made to the section sizes given in the design example. For simplicity, all chords were the same section size, and all webs were the same section size. As members designed for compression are more crucial, both top and bottom chords were selected as the top chord size (180 x 180 x 8.0 mm RHS), and webs as the compression diagonals (120 x 120 x 4.0 mm RHS). These members were checked for compactness according to AISC LRFD criteria for steel HSS (AISC, 2000).

$$\frac{b}{t} = 0.939 \sqrt{\frac{E}{F_y}} \tag{5.1}$$

The chord members are compact, but not the web members. Another possible compression diagonal size as given in the design example, a 100 x 100 x 5.0 mm RHS, met compactness criteria and was used for web members. Lateral bracings were sized to that of the webs.

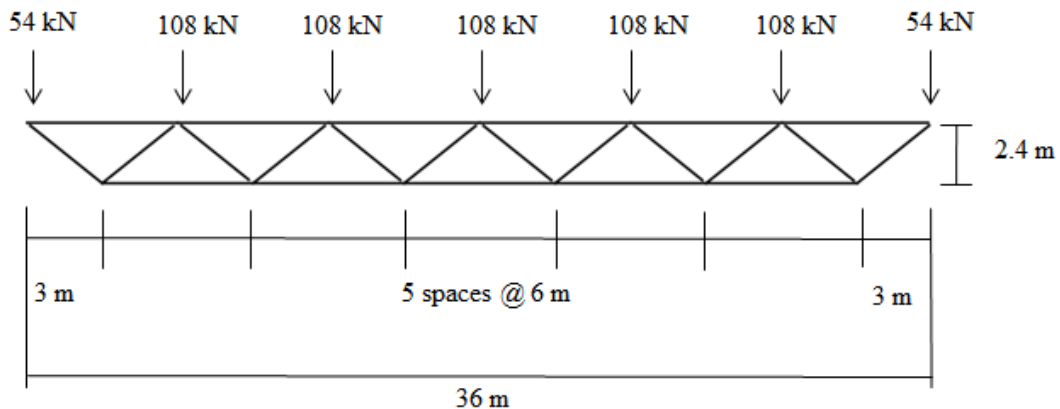


Figure 5-4: Truss design example layout by CIDECT

The truss design as given in Figure 5-4 fails by flexural buckling of the top chord in the center spans. Using Euler buckling (Eq. 24) where $K=0.9$ (AISC 2000), the axial force at buckling was determined to be 1726 kN. An elastic frame analysis was completed on the truss with loads applied as shown in Figure 5-4, and resulted in the top chord experiencing an 1143 kN compressive force. Therefore, the 2D truss should be able to withstand an applied load of 1.5 times the design loads.

$$P_{cr} = \frac{\pi^2 EI}{(KL)^2} \quad (5.2)$$

For all of the random variables considered, the nominal values, means, standard deviations, and distribution type are given in Table 10. For each truss, chord members were correlated and web members were correlated, hence all chords in a truss shared the same random values of E , F_y , t , and σ_r , and all webs shared their own value of E , F_y , t , and σ_r . Trusses were uncorrelated, so there were six unique trusses in the system. All chord and web members had their own unique randomly generated imperfection profile. Lastly, lateral bracings did not have random values as their strength is not crucial to the overall strength of the system, and were evaluated at the nominal values for the webs. Lateral bracings consisted of straight members running perpendicular to the trusses which connected the top chord panel points to the same panel point on the next truss, and diagonal bracings which connected the top chord panel points to the adjacent top chord panel points on the next truss to form a "V" shape (Figure 5-5).

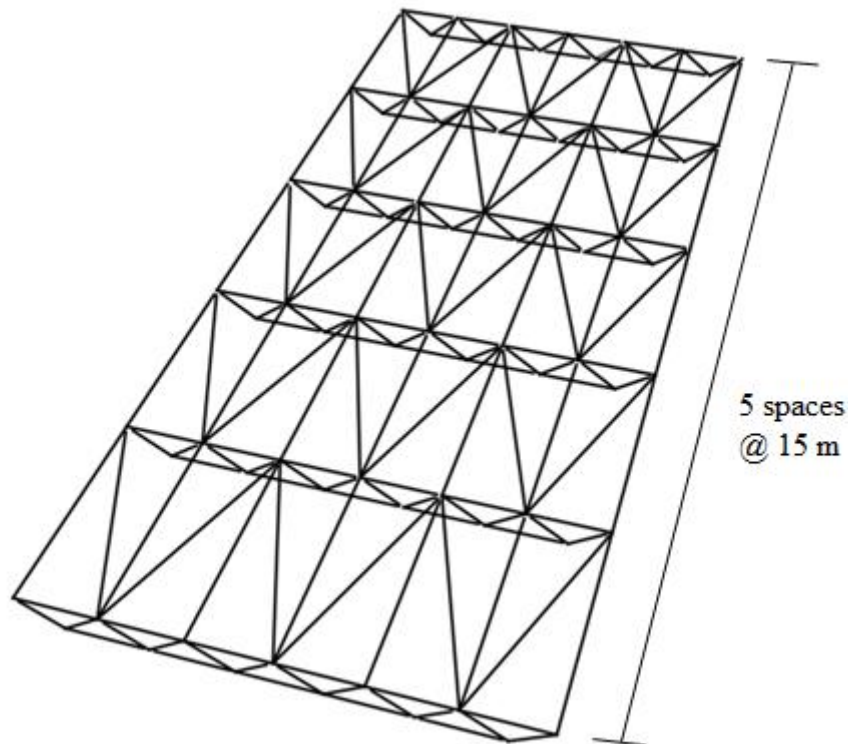


Figure 5-5: 3D truss system layout

The loads given in the design example are 108 kN at the interior panel points and 54 kN at the exterior panel points. For random loads, the applied load must be separated into live load and dead load. Assuming that live load is three times the dead load, and the load combination of $1.2D + 1.6L$ was utilized to calculate the 108 kN applied load, the un-factored dead load is 18 kN and the un-factored live load is 54 kN.

Table 5-2: Random variables in FE simulations

Variable	Nominal	μ	σ	distribution
t_c	8.0 mm	$0.964 * t_{nominal}$	0.039	Normal
t_w	5.0 mm			
E	200 GPa	$E_{nominal}$	$E_{mean} * 0.06$	Normal
F_y	0.35 GPa	$1.1 * F_{y_{nominal}}$	$F_{y_{mean}} * 0.1$	Normal
σ_r	0 (GPa)	$0.7 * F_{y_{mean}}$	0.05	Normal
δ_1/L	0	$1.26E-4$	$1.64E-4$	Lognormal
δ_2/L		$4.08E-5$	$5.16E-5$	
δ_3/L		$2.20E-5$	$2.81E-5$	
D	18 kN	$1.05 * D_{nominal}$	$D_{mean} * 0.10$	Normal
L	54 kN	$L_{nominal}$	$L_{mean} * 0.25$	Extreme type I

The truss systems were modeled in ABAQUS (2007) commercial finite element software using beam section elements type B31. Random variables were computed and input files written in MATLAB (Mathworks, 2011). The simulations were run on the Civil Engineering department's computing cluster at Johns Hopkins University.

6 SYSTEM RELIABILITY

6.1 BACKGROUND

The load and resistance (LRFD) specification uses load and resistance factors to obtain a target reliability (Eq. 6.1).

$$\phi R_n \geq \sum_i \gamma_i Q_{ni} \quad (6.1)$$

Reliability is related to the probability of failure as follows:

$$p_f = \Phi\left(-\frac{\mu}{\sigma}\right) = \Phi(-\beta) \quad (6.2)$$

where Φ is the standard normal cumulative distribution function. Specifying a target reliability index, $\beta = \beta_T$, enforces a uniform probability of failure. The current LRFD factors assume a member-based design and there is a resistance factor, ϕ , for each loading condition and type of failure. In component based design, all members and connections must be checked for all limit states, which is not an efficient process. Additionally, different members have various β , such as between 3 to 4 for beams, and 6 to 8 for fasteners (Nowak and Collins, 2000), which was a result of the calibration of LRFD to ASD. Designing to a target β for all cases will increase efficiency as no member or connection will be excessively over or under-designed. However, designing on a component basis does not accurately capture the system effect.

A system in which all members and connection meet β_T will not necessarily have a system where $\beta = \beta_T$. This is because there is a complex interaction between members and connections in a system, with varying levels of load redistribution among the members. In order to meet β_T for the system, advanced analysis must be performed. The AISC LRFD specification (2005) allows for direct 2nd order analysis (Appendix 7). The resistance factor for the system to meet β_T is different than that of an individual component's limit state resistance factor. The derivation for calculating the resistance factor is shown below.

The load effect Q on a structure and the resistance factor R are considered to be statistically independent random variables. The probability of failure is the probability that $R < Q$. This can be expressed as a single frequency distribution curve which combines the uncertainties in R and Q by dividing $R < Q$ by Q and expressing the result logarithmically (AISC, 1986). Therefore, the probability of failure is equal to the probability that the indicator function, g , is less than zero as shown in Eq. 6.3 where the subscript m denotes the mean value.

$$g = \ln\left(\frac{R_m}{Q_m}\right) \leq 0 \quad (6.3)$$

The reliability index is the mean divided by the standard deviation of the indicator function g and is calculated in Eq. 6.4.

$$\beta = \frac{R_m - Q_m}{\sqrt{\sigma_R^2 + \sigma_Q^2}} \quad (6.4)$$

Using small-variance approximations (Ellingwood et al., 1980), β is solved for as follows where V is the coefficient of variation:

$$\beta = \frac{\ln\left(\frac{R_m}{Q_m}\right)}{\sqrt{V_R^2 + V_Q^2}} \quad (6.5)$$

Rearranging to separate the means of resistance and load effects:

$$\mu_R = \exp\left(\beta\sqrt{V_R^2 + V_Q^2}\right)\mu_Q \quad (6.6)$$

The substitution below is made (AISC, 1986):

$$\sqrt{V_R^2 + V_Q^2} \approx V_Q + \alpha V_R \quad (6.7)$$

Substituting Eq. 6.7 into Eq. 6.6 and rearranging yields:

$$\exp(-\alpha\beta V_R)\mu_R = \exp(\beta V_Q)\mu_Q \quad (6.8)$$

The resistance factor R is expressed in Eq. 6.9, where M is the variation in strength of the material, F is the variation in fabrication, and P is the variation due to the methods of analysis. The load effect Q is expressed in Eq. 34, where A is the variation in load, B is the variation due to the mode in which the load acts, and C is the variation due to the methods of analysis (Nowak and Collins, 2000). The subscript n denotes the nominal value.

$$R = P \cdot M \cdot F \cdot R_n \quad (6.9)$$

$$Q = A \cdot B \cdot C \cdot Q_n \quad (6.10)$$

Solving for V_R , μ_R , V_Q , μ_Q and substituting into Eq. 6.8 yields Eq. 6.11:

$$\exp\left(-\alpha\beta\sqrt{V_P^2 + V_M^2 + V_F^2}\right)\mu_P\mu_M\mu_F R_n = \exp\left(\beta\sqrt{V_A^2 + V_B^2 + V_C^2}\right)\mu_A\mu_B\mu_C Q_n \quad (6.11)$$

which is now in the LRFD format as shown below:

$$\phi R_n = \gamma Q_n \quad (6.12)$$

The resistance factor is computed as shown in Eq. 6.13. This is the resistance factor as given in AISC LRFD, 1986.

$$\phi = \mu_P\mu_M\mu_F \exp\left(-\alpha\beta\sqrt{V_P^2 + V_M^2 + V_F^2}\right) = \left(\frac{R_m}{R_n}\right) \exp(-\alpha\beta V_R) \quad (6.13)$$

Results from the simulations yielded values for R_m , R_n , and V_R . The resulting resistance factor for the system was then calculated.

6.2 PROPOSED SYSTEM RELIABILITY METHOD

The procedure for determining a system resistance factor is as follows:

- 1) Determine strength limit state (in this case it is ultimate capacity).
- 2) Choose a truss geometry and layout and calculate nominal loads.
- 3) Check design to existing specifications to make sure it is not excessively over or under-designed.
- 4) Identify the random variables affecting strength, choose a load combination, and apply loads using a load increment factor.

- 5) Run an advanced analysis using nominal values of all random variables. The load increment factor causing failure is denoted λ_{un} .
- 6) Run simulations varying the random variables. For each simulation, the load increment factor causing failure is denoted λ_u .
- 7) Determine the mean and C.O.V of λ_u/λ_{un} (Eq. 6.14 and 6.15). These are the statistics of the resistance.

$$R_m/R_n = \left(\lambda_u/\lambda_{un} \right)_m \quad (6.14)$$

$$V_R = COV \left(\lambda_u/\lambda_{un} \right) \quad (6.15)$$

- 8) Determine the system resistance factor using the statistics for the resistance (Eq. 6.13) where $\alpha=0.55$ and $\beta=3$ (AISC, 1986).

$$\phi = \left(R_m/R_n \right) \exp \left((-0.55)(3)V_R \right) \quad (6.16)$$

- 9) For the given value of ϕ , determine the probability of failure (p_f) and the reliability index, β . This is done by running advanced analysis of the simulations with random variables affecting the strength and random loads for the specific load combination. A load increment factor, λ , is applied to the factored loads until the strength limit state is reached. This value is denoted λ_{max} .
- 10) Plot the distribution of λ_{max} . The failure condition is defined in Eq. 6.17. The probability of failure is obtained from the cumulative distribution function of the fitted distribution.

$$failure = \lambda_{max} - 1 = 0 \quad (6.17)$$

- 11) Calculate the reliability index resulting from the probability of failure. This is computed by taking the inverse of the standard normal CDF (Eq. 6.18).

$$\beta = -\Phi^{-1} \left(p_f \right) \quad (6.18)$$

The above method is useful to calculate the actual system reliability. This calculated β is the system reliability of a system designed based on individual components. To design a system with a specified target reliability, β_T , continue with the following steps:

- 12) If the calculated β does not equal the target β_T , the structure needs to be redesigned. This could involve the use of a different section, or alternatively as was done herein, the thickness of all members was scaled. The redesign should satisfy Eq. 6.19.

$$(\phi') \lambda_{max} = 1 \quad (6.19)$$

- 13) Repeat steps 9-12 until the target β_T is met, or close enough to obtain an accurate estimate using linear interpolation. The value of ϕ corresponding to β_T is the system resistance factor.

Repeat this procedure for various load combinations. For the gravity case, the load increment factor is applied to the factored dead and live loads (Eq. 6.20). For the wind or snow dominated load case, the gravity component due to dead and live loads is considered constant, and the load increment factor is applied to either the factored wind or snow load component (Eq. 6.21 – 6.22). These are the load combinations for LRFD

where load combination models the design load when one load component is at its maximum value and the others are taken at their arbitrary-point-in-time values (AISC, 2005). Thus only one load component is scaled until failure while the others remain at their arbitrary-point-in-time values. While this does simplify the loading conditions, it is necessary as directly simulating the loading conditions along with all the variations affecting resistance would be too cumbersome a process.

$$\lambda(D+L) \tag{6.20}$$

$$D+L_{apt} + \lambda(S) \tag{6.21}$$

$$D+L_{apt} + \lambda(W) \tag{6.22}$$

6.3 VARILIBLTY IN RESISTANCE

The following is an implementation of steps 5-8 of the above procedure (steps 1-4 were previously completed) for the gravity controlling load combination. The truss simulations included random variables affecting resistance only; loads were taken at their nominal values. Results from simulations of 2D and 3D models with loads applied at the top chord and bottom chord were completed.

Below are the histograms and PDF fits for simulations ran with random variables affecting the resistance, but loads at their nominal values. The load proportionality factor, LPF, also denoted λ_{max} above, was the load increment factor applied to the factored loads until the strength limit state was reached for each simulation. Figure 6-1 shows the results of the 2D simulations, Figure 6-2 shows the results of the 3D simulations with loads applied at the top chord, and Figure 6-3 shows the results of the 3D simulations with loads applied at the bottom chord. For the 3D simulations, both simulation sets (loads applied at TC and BC) had the same set of random truss structures generated, only the load application point changed. This was done to analyze of the effects of lateral bracings on the lateral torsional buckling failure mode. The results of the simulations and probability of failure and β calculated from the fitted distributions are given in Table 6.1

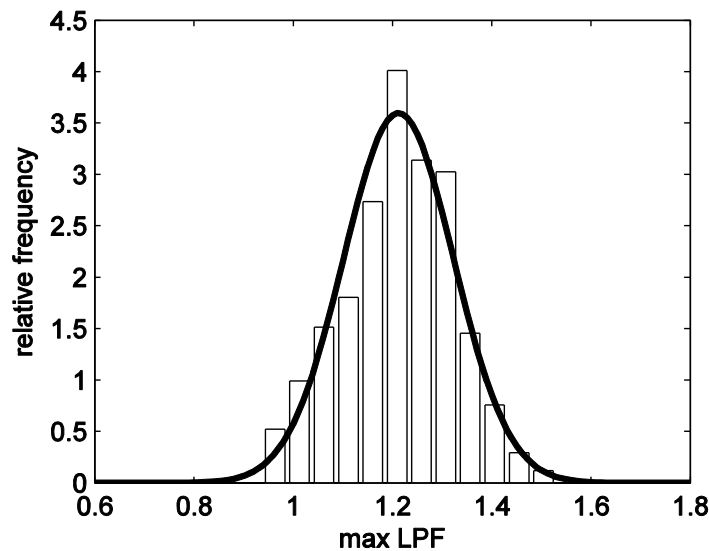


Figure 6-1: Histogram and normal PDF fit of maximum load proportionality factors for 2D truss simulations

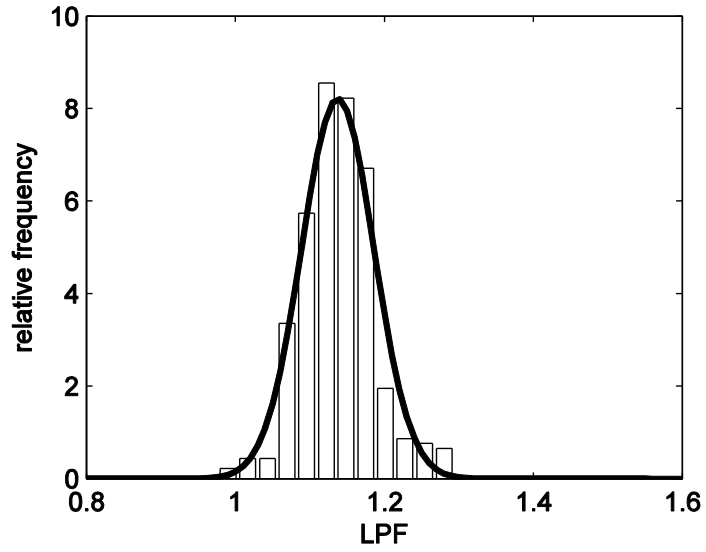


Figure 6-2: Histogram and normal PDF fit of maximum load proportionality factors for 3D truss simulations with loads at top chord

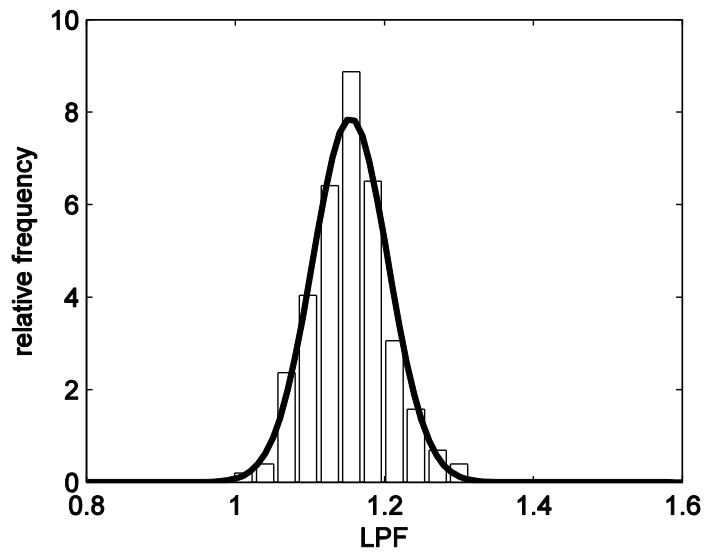


Figure 6-3: Histogram and normal PDF fit of maximum load proportionality factors for 3D truss simulations with loads at bottom chord

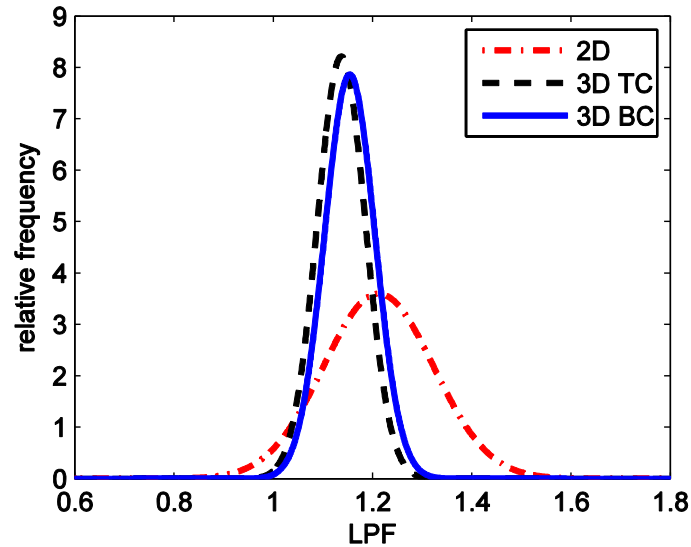


Figure 6-4: PDFs of maximum load proportionality factors for 2D, 3D load at top chord, and 3D load at bottom chord truss simulations with nominal loads

Table 6-1: Results of simulations with nominal loads

	2D	3D_TC	3D_BC
Nominal	1.500	1.498	1.508
μ	1.212	1.137	1.154
$\mu/\text{nominal}$	0.808	0.759	0.765
σ	0.111	0.049	0.051
V	0.091	0.043	0.051
P_f	0.0281	0.0024	0.0013
β	1.91	2.82	3.01

The 3D simulations have a higher β than the 2D simulations. This is not because the 3D system is stronger, as the nominal maximum λ is about equal for 2D and 3D simulations. Instead, this is a result of the decreased variance in the 3D simulations. The variance in the maximum load decreased about 55% in the 3D system versus the 2D system.

6.4 FAILURE MODES AND SYSTEM EFFECTS

The 2D nominal truss failed due to flexural buckling in the center top chord at a load proportionality factor of 1.5. This matches the prediction based on design calculations. In the 2D simulations including random variations affecting strength, the weaker trusses failed by flexural buckling in one of the center top chords, while the stronger trusses failed by flexural buckling in both center top chords, and were able to experience larger deflections. Figure 6.5(a) shows the load proportionality factor versus the vertical deflection at the center of the bottom chord for three of the 2D simulations: the strongest, the weakest, and a mid-strength truss.

In the 3D simulations, the trusses also failed in the top chord of one or both of the middle trusses. Figure 6.5(b) shows the load proportionality factor versus the vertical deflection at the center of the bottom chord for one of the middle trusses. Most of the trusses experienced about the same vertical deflection, however out-of-plane displacements varied based on the strength of the truss. Figure 6.6 shows the load proportionality factor versus horizontal displacements at the center of the bottom chord for one of the middle trusses. Strong trusses experienced no out-of-plane displacements, while mid-strength trusses experienced a small deflection, and weak trusses experienced out-of-plane deflections after reaching their maximum load.

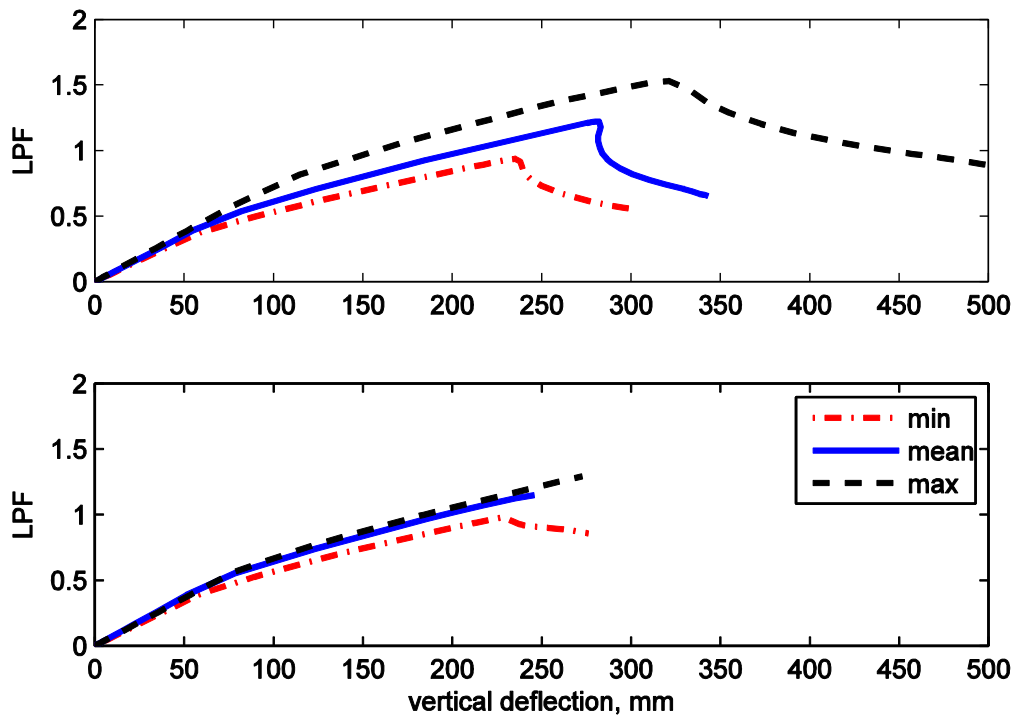


Figure 6-5: Load proportionality factor versus vertical deflection at BC for (a) 2D simulations and (b) 3D simulations

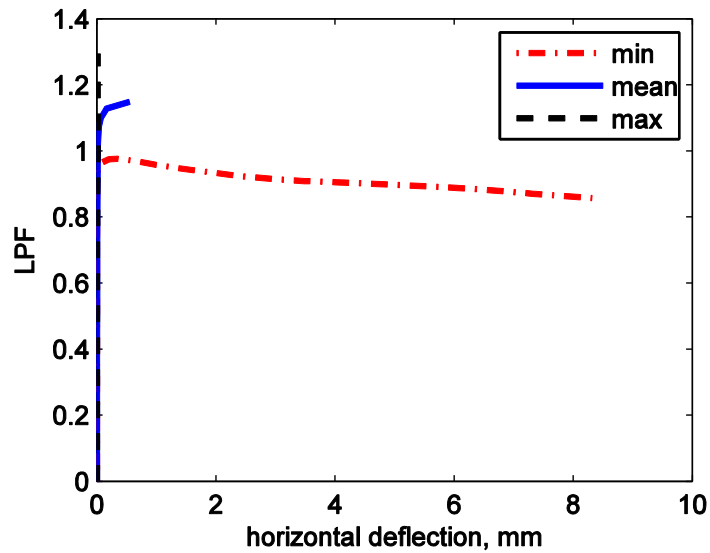


Figure 6-6: Load proportionality factor versus horizontal deflection at BC for 3D simulations

Results for the 3D simulations with loads applied at the top chord or bottom chord were close, but those due to load applied at the bottom chord were slightly improved. This is because loads applied at the bottom chord help to counteract the movement of the truss in the out-of-plane direction, while loads applied at the top chord increase the instability. Since overall the results were close, it was determined that the lateral bracing at the top chord was sufficient.

It is important to note the effect of proper lateral bracings. If the system is not properly braced, it will fail by lateral torsional buckling. A set of simulations was completed without diagonal lateral bracings, but with only the bracings perpendicular to the top chord. The mean max load increment factor was $\lambda = 0.953$ for this set, and the failure mode was out-of-plane lateral torsional buckling. Without proper lateral bracings, the system was worse than that of a single truss in 2D, and as the mean max λ was less than 1, over half of the random systems did not even resist nominal loads. Although the individual members are square HSS and have the same properties about both axes, as a system it has a strong axis and a weak axis. The truss can be analyzed as a beam consisting as a W shape, where the top and bottom chords are the flanges, and the diagonals act as a thin web. Therefore, the system is very weak in resisting out-of-plane bending and must be braced accordingly, while it is much stronger in resisting in-plane bending. This shows the importance of understanding how to properly brace a system.

The 3D truss system is a system of random 2D trusses. To determine the system's behavior, the probability of failure found by the 3D simulations was compared to the probability of failure from an ideal series system (Eq. 6.23) and an ideal parallel system (Eq. 6.24):

$$p_{f(\text{series})} = 1 - (1 - p_f)^n \quad (6.23)$$

$$P_{f(\text{parallel})} = (p_f)^n \quad (6.24)$$

where p_f is the probability of failure of the random 2D truss, which is given in Table 6.2 ($p_f=0.0281$). Using the above equations, $p_{f(\text{series})}=0.1572$ and $p_{f(\text{parallel})}=4.923E-10$. The $p_{f(\text{system})}$ found in the 3D simulations is given in Table 6.2 ($p_{f(\text{system})}=0.0024$). The 3D system is able to redistribute some of the load, however it is much closer in behavior to that of a series system than that of a parallel system. This is not surprising as trusses are typically categorized as series systems (Nowak and Collins, 2000).

6.5 VARIABILITY IN RESISTANCE AND LOAD

The data presented below is for simulations with random variables affecting the resistance of the system as well as random loads for the gravity controlling load combination. This includes procedure steps 9-13. All trusses herein had loads applied at the top chord panel points. Figure 6-7 is the histogram and PDF fit for the 2D simulations, while Figure 6-8 is that of the 3D simulations. Results of the simulations as well as calculated probability of failure and β are given in Table 6-2.

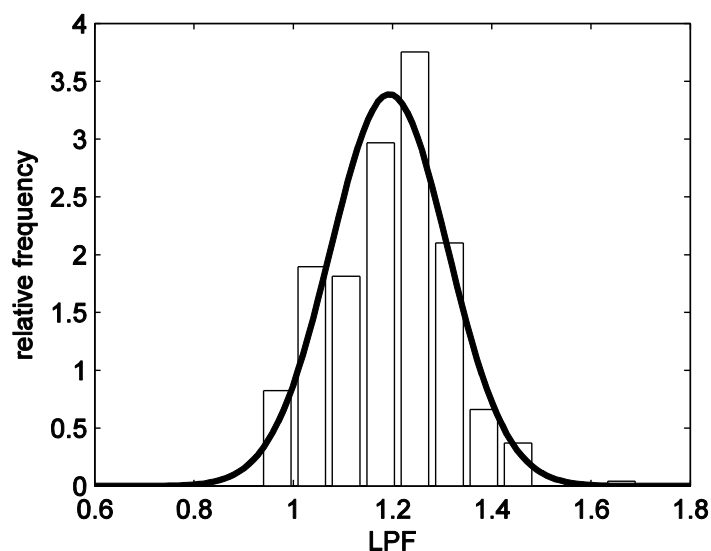


Figure 6-7: Histogram and normal PDF fit of maximum load proportionality factors for 2D truss simulations with random loads

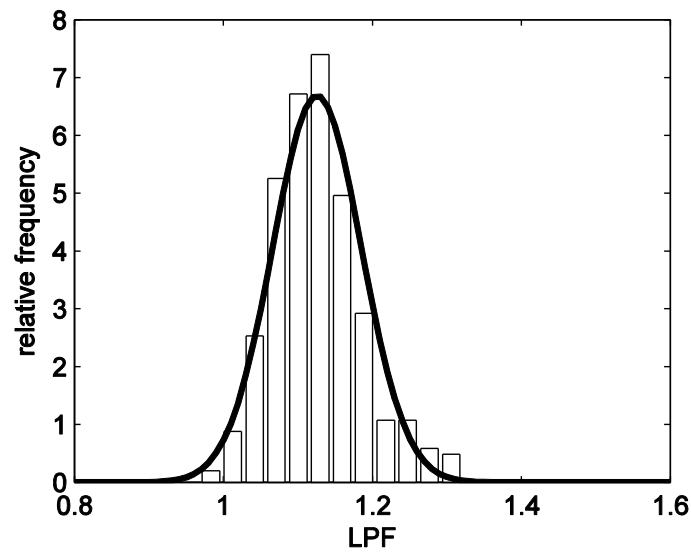


Figure 6-8: Histogram and normal PDF fit of maximum load proportionality factors for 3D truss simulations with random loads at top chord

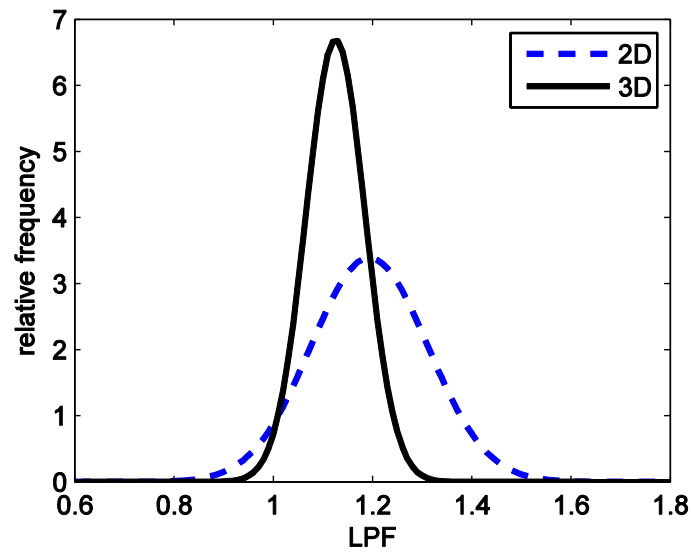


Figure 6-9: PDFs of maximum load proportionality factors for 2D and 3D truss simulations with random loads at top chord

Once again, the 2D simulation results have a larger spread than the 3D, and thus a lower β value. Additionally, for both 2D and 3D results, the β value is lower when incorporating random loads than the simulations with nominal loads. For the 3D simulations $\beta=2.11$, which is lower than the target value of $\beta=3$. The truss was redesigned by increasing the thickness of the chord members, as the chord was the critical member to fail first. Simulations were completed for $t_c=9.0\text{mm}$, and the resulting histogram is shown in Figure 6-10 and results in Table 6-2. This yielded $\beta=3.83$, which is above the target value. Using linear interpolation, it was estimated that a $t_c=8.5\text{mm}$ would yield the target $\beta_T=3.0$, so another set of simulations was completed for $t_c=8.5\text{mm}$. The histogram of results is shown in Figure 6-11 and results given in Table 6-2.

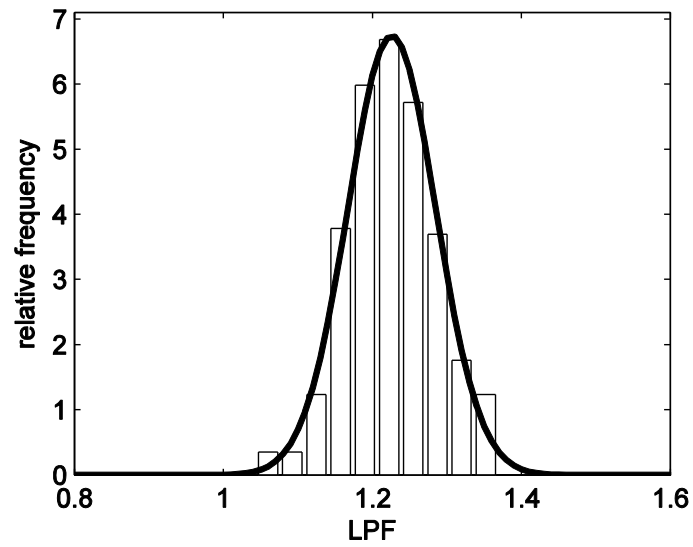


Figure 6-10: Histogram and normal PDF fit of maximum load proportionality factors for redesigned 3D truss ($t_c=9.0\text{mm}$) simulations with random loads at top chord

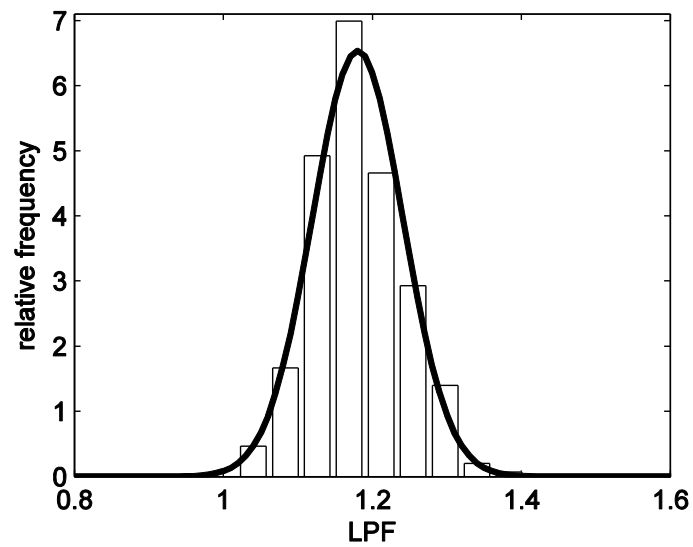


Figure 6-11: Histogram and normal PDF fit of maximum load proportionality factors for redesigned 3D truss ($t_c=8.5\text{mm}$) simulations with random loads at top chord

Table 6-2: Results of simulations with all random variables considered

	2D ($t_c=8\text{mm}$)	3D_TC ($t_c=8\text{mm}$)	3D_TC ($t_c=9\text{mm}$)	3D_TC ($t_c=8.5\text{mm}$)
Nominal	1.500	1.498	1.684	1.598
μ	1.193	1.126	1.226	1.180
$\mu/\text{nominal}$	0.795	0.752	0.728	0.738
σ	0.118	0.060	0.059	0.061
V	0.099	0.053	0.048	0.052
P_f	0.0505	0.0173	6.39E-5	0.0016
β	1.64	2.11	3.83	2.95
ϕ_s	0.676	0.688	0.672	0.678

The redesign of the truss system with a top chord thickness of 8.5mm (was originally 8.0mm) gave a close reliability index to the target value. The resistance factor associated with $\beta=3.0$ should be about the same for that of $\beta=2.95$. Therefore, the system resistance factor for the gravity load combination (1.2D + 1.6L) is given as $\phi=0.678$. This is a lower resistance factor than is typical for a single component ($\phi=0.75 - 0.9$). A lower resistance factor requires a larger nominal resistance so that Eq. 6.1 remains true. Therefore, designing as a system would require the structure to have a higher nominal resistance, which would usually be fulfilled by larger section sizes, hence greater material costs.

This roof system is not likely not be controlled by wind load, however depending on the location snow load may be a controlling load combination. Therefore, the system reliability analysis should be completed for the load combination given in Eq. 6.22.

7 CONCLUSIONS

The work presented herein is a formwork for determining a system resistance factor to meet a target reliability index in LRFD format. Current design specifications apply a resistance factor to each member and connection; however this fails to reflect system behavior. In order to obtain the desired reliability index, a system resistance factor must be used instead of a member resistance factor.

Finite element models were created and analyzed using an advanced second order analysis. The specific system analyzed herein, a system of 2D trusses composed of HSS members connected with lateral bracings, had a higher reliability index, hence lower probability of failure than a single 2D truss. This was not a result of a change in mean strength from 2D to 3D, but rather due to a reduction in variance of 50% for the 3D system. The 3D system was an improvement over the 2D system, however there could be further improvements if the system were redesigned to more closely resemble that of a parallel system. Overall, the system resistance factor for both 2D and 3D was lower than that of individual components ($\phi=0.75 - 0.90$ depending on the component).

It is important to collect data for all variables affecting resistance and load in order to reflect real structures. Random variable data collected that affected resistance included geometric member imperfection, thickness, Young's modulus, yield stress, and residual stresses. Member imperfection profiles were generated based on measurements found in literature. Imperfections were significantly smaller than the maximum permissible tolerance of $L/1000$. Distributions of residual stresses in HSS based on measurements in literature were presented. For other types of structures and materials, additional data will be needed on random variables affecting the desired limit state. Random loads were implemented through AISC's (2005) load combinations.

Large scale simulations and models are becoming less computationally expensive to perform as computing technology improves. Design will shift away from a component based design towards system design by advanced second order analysis. It is the goal that system design will more accurately reflect real structural behavior and lead to safer designs, as well as promote innovation in design. Enforcing a uniform reliability, hence uniform probability of failure, will increase safety in systems which are under-designed and increase efficiency in those which are currently over-designed. Shifting the mindset away from a critical member design to a system design approach will enable engineers to deviate from the standard structural configurations and innovate on new ones.

8 REFERENCES

ABAQUS, *ABAQUS/Standard Version 6.7-1*, D. Systemes, Editor 2007.

American Institute of Steel Construction (AISC), (1986). *Load and Resistance Factor Design Manual of Steel Construction*, 1st ed., Chicago.

American Institute of Steel Construction (AISC), (2000). *Load and Resistance Factor Design Specification for Steel Hollow Structural Sections*, Chicago.

American Institute of Steel Construction (AISC), (2005). *Steel Construction Manual*, 13th ed., Chicago.

Association of Steel Construction on Milan, (1966). "Test Certificate for Column Buckling, Short Column Tests, and Traction Tests." Institute of Constructional Science, Milan University of Technology (Politecnico), Milan.

Blum, Hannah B. (2012). "Framework for determining system resistance factors in LRFD using advanced second order analysis for HSS truss systems." *Master's Thesis, Johns Hopkins University*, Baltimore, Maryland, USA.

Buonopane, Stephen G. (2008). "Strength and Reliability of Steel Frames with Random Properties." *Journal of Structural Engineering*, 134(2), 337-344.

Buonopane, S. G. and Schafer, B. W. (2006). "Reliability of Steel Frames Designed with Advanced Analysis." *Journal of Structural Engineering*, 132(2), 267-76.

Coutie, et. al. (1987). "Testing of full scale lattice girders fabricated with RHS members", *University of Nottingham*. In *Structural Assessment – the use of full and large scale testing*, pages 98-105. Edited by Garaset. al., London, UK.

Clarke, M. J. et al., (1992). "Advanced Analysis of Steel Building Frames." *Journal of Constructional Steel Research*, 23, 1-29.

Cran, J. A., (1989). "The Engineer's Guide to Hollow Sections." *Proc., Canadian Society for Civil Engineering Annual Conference*, St. John's, Newfoundland.

Davison, T. A. and Birkemoe, P. C. (1982). "Column behavior of cold-formed hollow structural steel shapes." *Canadian Journal of Civil Engineering*, 10, 125-141.

De Koning, C. H. M., and Wardenier, J., (1979). *Tests on Welded Joints in Complete Girders Made of Square Hollow Sections*, Stevin Laboratory, Department of Civil Engineering, Delft University of Technology, Delft, TheNetherlands.

Dumonteil, Pierre, (1989). "In-Plane Buckling of Trusses." *Canadian Journal of Civil Engineering*, 16, 504-518.

Ellingwood, Bruce R., (2000). "LRFD: implementing structural reliability in professional practice." *Engineering Structures*, 22, 106-115.

Ellingwood, Bruce et al., (1980). *Development of a Probability Based Load Criterion for American National Standard A58, Building Code Requirements for Minimum Design Load in Buildings and Other Structures*, U.S. Department of Commerce / National Bureau of Standards, Gaithersburg, MD.

Ellingwood, Bruce and Galambos, Theodore V., (1982). "Probability-Based Criteria for Structural Design." *Structural Safety*, 1, 15-26.

Ellingwood, Bruce and O'Rourke, Michael, (1985). "Probabilistic Models of Snow Loads on Structures." *Structural Safety*, 2, 291-299.

Ellingwood, Bruce and Redfield, Robert, (1983). "Ground Snow Loads for Structural Design." *Journal of Structural Engineering*, 109, 950-964.

- Frater, George S., (1991). *Performance of Welded Rectangular Hollow Structural Section Trusses*, PhD Thesis, University of Toronto.
- Frater, George S., and Packer, Jeffery A., (1992). "Modeling of Hollow Structural Section Trusses." *Canadian Journal of Civil Engineering*, 19, 947-959.
- Galambos, Theodore V. and Racindra, Mayasandra K., (1978). "Properties of Steel for Use in LRFD." *Journal of the Structural Division*, 104(9), 1459-1468.
- Giddings, T. W., and Wardenier, J., (1986). *CIDECT Monograph No 6 – The Strength and Behaviour of Statically Loaded Welded Connections In Structural Hollow Sections*, CIDECT, Great Britain.
- Haldar, A., and Mahadevan, S. (2000). *Probability, Reliability and Statistical Methods in Engineering Design*, John Wiley and Sons, Inc., New York.
- Hasan, S. W., and Hancock, G. J. (1989). "Plastic Bending Tests of Cold-Formed Rectangular Hollow Sections." *Journal of Steel Construction*, 23(4), 2-19.
- Kato, B. and Aoki, H. (1978). "Residual Stresses in Cold-Formed Tubes." *Journal of Strain Analysis*, 13(4), 193-204.
- Key, Peter W., (1988). *The Behaviour of Cold-Formed Square Hollow Section Columns*, PhD Thesis, School of Civil and Mining Engineering, University of Sydney.
- Key, Peter W. and Hancock, Gregory J. (1993). "A Theoretical Investigation of the Column Behaviour of Cold-Formed Square Hollow Sections." *Thin-Walled Structures*, 16, 31-64.
- Korol, R. M., and El-Zanaty, M., (1977). "Unequal Width Connections of Square Hollow Sections in Vierendeel trusses." *Canadian Journal of Civil Engineering*, 4, 190-201.
- Korol, Robert M., and Mirza, Farooque A., (1982). "Finite Element Analysis of RHS T-Joints." *Journal of the Structural Division*, September, 2081-2098.
- Li, S.H. et al. (2008). "Residual stresses in roll-formed square hollow sections." *Thin-Walled Structures*, 47, 505-513.
- Mathworks, Matlab 5.13.0 (R2011b). Mathworks, Inc., (www.mathworks.com), 2011.
- Moen, Christopher D., et al. (2008). "Prediction of residual stresses and strains in cold-formed steel members." *Thin-Walled Structures*, 46, 1274-1289.
- Nowak, Andrzej S. and Collins, Kevin R., (2000). *Reliability of Structures*, The McGraw Hill Companies, Inc., New York.
- Packer, Jeffery A., (1986). "Design Examples for HSS Truss." *Canadian Journal of Civil Engineering*, 13, 460-473.
- Packer, J. A., and Davis, G., (1989). "On the Use and Calibration of Design Standards for SHS Joints." *The Structural Engineer*, 67(21), 377-386.
- Packer, Jeffery A., (1993). "Moment Connections Between Rectangular Hollow Sections." *Journal of Constructional Steel Research*, 25, 63-81.
- Packer, et. al., (2009). *Design Guide for Rectangular Hollow Section (RHS) Joints Under Predominantly Static Loading*, 2nd ed., CIDECT, Germany.
- Packer, J. A., and Henderson, J. E. (1997). *Hollow Structural Section – Connections and Trusses*, 2nd Ed., Canadian Institute of Steel Construction, Vancouver, BC.

- Saidani, Messaoud, (1991). *Joint Flexibility on Rectangular Hollow Section Trusses*, PhD Thesis, Department of Civil Engineering, University of Nottingham.
- Saidani, M., (1998). "The Effect of Joint Eccentricity on the Distribution of Forces in RHS Lattice Girders." *Journal of Constructional Steel Research*, 47, 211-221.
- Sherman, Donald R. (1969). "Residual Stress Measurements in Tubular Members." *Journal of the Structural Division*, 95(4), 635-647.
- Szlendak, J., (1991). "Beam-Column Welded RHS Connections." *Thin-Walled Structures*, 12, 63-80.
- Tong, Lewei, et al. (2012). "Experimental investigation on longitudinal residual stresses for cold-formed thick-walled square hollow sections." *Journal of Constructional Steel Research*, 73, 105-116.
- Wardenier, J. (1982). *Hollow Section Joints*, Delft University Press, Delft, The Neatherlands.
- Wardenier, et. al., (2010). *Hollow Sections in Structural Applications*, CIDECT, Delft, The Neatherlands.
- Wilkinson and Hancock, (1997). *Tests for the Compact Web Slenderness of Cold-Formed Rectangular Hollow Sections*, *Research Report R744*, Centre for Advanced Structural Engineering, Department of Civil Engineering, The University of Sydney.